Degradation processes of reinforced concretes by combined sulfate–phosphate attack

Michele Secco [a,b,*], Giulio Isacco Lampronti [c], Moritz-Caspar Schlegel [d,e], Lara Maritan [f], Federico Zorzi [f]

[a] Inter-Departmental Research Center for the Study of Cement Materials and Hydraulic Binders (CIRCe), University of Padova, Via Gradenigo 6, 35131 Padova, Italy
[b] Department of Civil, Environmental and Architectural Engineering (ICEA), University of Padova, Via Marzolo 9, 35131 Padova, Italy
[c] Department of Earth Sciences, University of Cambridge, Downing Street, CB2 3EQ Cambridge, United Kingdom
[d] BAM Federal Institute for Materials Research and Testing, Unter den Eichen 87, 12205 Berlin, Germany
[e] Helmholtz-Zentrum Berlin fürMaterialien und Energie GmbH, Hahn-Meitner-Platz 1, 14109 Berlin, Germany
[f] Department of Geosciences, University of Padova, Via Gradenigo 6, 35131 Padova, Italy

ARTICLE INFO

ABSTRACT

A novel form of alteration due to the interaction between hydrated cement phases and sulfate and phosphate-based pollutants is described, through the characterization of concrete samples from an industrial reinforced concrete building. Decalcification of the cement matrices was observed, with secondary sulfate and phosphate-based mineral formation, according to a marked mineralogical and textural zoning. Five alteration layers may be detected: the two outermost layers are characterized by the presence of gypsum–brushite solid solution phases associated with anhydrous calcium sulfates and phosphates, respectively, while a progressive increase in apatite and ammonium magnesium phosphates is observable in the three innermost layers, associated with specific apatite precursors (brushite, octacalcium phosphate and amorphous calcium phosphate, respectively). The heterogeneous microstructural development of secondary phases is related to the chemical, pH and thermal gradients in the attacked cementitious systems, caused by different sources of pollutants and the exposure to the sun's radiation.

1. Introduction

1.1. Scientific background

The alteration of concrete structural elements due to the action of external chemical degrading agents is one of the main causes for the reduction of the service life in modern constructions [1]. These dynamics are particularly aggressive in environments characterized by heavy soil and atmospheric pollution, leading to a progressive decalcification of the cementitious matrix and oxidation of the rebars [2,3]. Among the various forms of concrete chemical degradation, the external sulfate attack has been widely studied over the last two decades. Several theories on the actual contribution of this alteration dynamic on the physical and mechanical decay of concrete structures have been formulated [4–6]. Furthermore, the leaching and decalcification processes due to the exposure of concrete to acidic solutions have been extensively investigated in several scientific studies [7–10]. Such chemical alteration dynamics are extremely detrimental to the durability of cement-based materials, leading to the dissolution of cement hydration products – mainly portlandite and C–S–H – and consequent loss of concrete strength.

Yet, there are few literature references on phosphate attack in cementitious materials, despite the interactions between phosphate ions and calcium-saturated systems that are widely demonstrated [11–13]. Some authors refer to limited decalcification on hydrated cement pastes under the action of phosphoric acid [14]. Moreover, an experimental and modeling study on concrete samples in contact with phosphate-rich solutions has been carried out to assess potential phosphate ion–concrete interactions [15]. The results of this integrated study showed that, while the formation of apatite on the expense of portlandite is thermodynamically favored in such systems, this mineral phase is not found experimentally, most likely due to kinetic factors. Nevertheless, the interaction between phosphates and concrete has never been evaluated on systems far from equilibrium characterized by local pH and chemical concentration gradients, corresponding to actual situations in attacked concrete structures materials. Moreover, the interaction between phosphate ions and other chemical species (e.g. sulfates) in case of concrete degradation by several types of chemical pollutants has never been taken into consideration before, as well as the possible evolution of the altered cementitious systems under variable temperature regimes, typical for temperate climates.

As for the influence of pH in the evolution of a hypothetical phosphate-related alteration of concrete, several studies confirmed

* Corresponding author at: Via Gradenigo 6, 35131 Padova, Italy. Tel.: +39 0498279169.
E-mail addresses: michele.secco@unipd.it (M. Secco), gil21@cam.ac.uk (G.I. Lampronti), moritz-caspar.schlegel@helmholtz-berlin.de (M.-C. Schlegel), lara.maritan@unipd.it (L. Maritan), federico.zorzi@unipd.it (F. Zorzi).

the strong correlation between this parameter and the type of calcium phosphate phase formed [16–18]. The most common and least soluble mineral, hydroxyapatite ($Ca_5(PO_4)_3(OH)$, commonly abbreviated HAP), is stable under neutral or basic conditions [17]. On the other hand, phases such as brushite ($Ca(HPO_4)\cdot2(H_2O)$, commonly abbreviated as DCPD) and octacalcium phosphate ($Ca_8(HPO_4)_2(PO_4)_4\cdot5(H_2O)$, commonly abbreviated as OCP) are generally crystallized from more acidic solutions [16,18]. Both brushite and octacalcium phosphate are reported to be precursors of apatite at acidic and neutral pH, respectively [17]. The higher solubility and lower stability of the two phases with respect to apatite cause their progressive transformation into apatite, both by dissolution and re-precipitation processes and by epitaxial growth [17].

Apart from the alteration dynamics related to the sole calcium–phosphate ion interaction in concrete, it is necessary to take into account other mutual interactions between phosphate compounds, concrete constituents and other external chemical species. Regarding this topic, the possible synergic action of phosphate and sulfate-based pollutants toward the alteration of cement-based materials needs to be considered, due to the extensive literature devoted to the study of calcium phosphate and sulfate phases in solid solution [19–22]. Gypsum and brushite both belong to the monoclinic system and have similar structures, despite the fact that they are not isomorphous ($a = 5.182$ Å, $b = 15.180$ Å, $c = 6.239$ Å, $\beta = 116.43°$, sp.gr. $I2/a$ for brushite; $a = 5.670$ Å, $b = 15.201$ Å, $c = 6.533$ Å, $\beta = 118.60°$, sp.gr. $I2/c$ for gypsum [21]). Although they have different sizes (the phosphate group is larger than the sulfate one), the substitution of sulfate and phosphate groups can occur within certain limits [20], and a solid solution between the two phases, which also comprehends the stoichiometric mineral ardealite ($Ca_2(SO_4)(HPO_4)\cdot4(H_2O)$, monoclinic system, Cc space group), can form. Furthermore, it has been demonstrated [22] that the relative proportions between the two end members of the solid solution have relevant influences on the dehydration behavior of the resulting compounds, being significantly different from the ones of the pure end members within certain composition intervals. Supposedly, such behavior influences the evolution of the secondary phases in case of alteration of the concrete elements exposed to significant seasonal temperature variations [23], as it happens in temperate climates.

Furthermore, the interaction between phosphate ions, nitrogen-based pollutants and magnesium ions deriving both from concrete cementitious matrix and aggregate fraction, needs to be considered, both due to the extensive scientific literature regarding the detrimental action of ammonium salts on concrete [24–26] and the occurrence of ammonium phosphate phases like struvite under certain chemical–physical conditions. Struvite ($(NH_4)MgPO_4\cdot6(H_2O)$) is a hydrated phase consisting of magnesium, ammonium and phosphate in equal molar concentrations. Ammonium can be substituted to a certain extent by alkaline ions, in particular potassium [27]. Struvite precipitation is controlled by pH, degree of supersaturation, temperature and the presence of other ions in solution such as calcium, and can occur when the concentrations of magnesium, ammonium and phosphate ions exceed the solubility product for struvite. Among the various factors, pH is crucial for the formation of this phase, being sparingly soluble in neutral and alkaline, but readily soluble in acid conditions [28].

Finally, the possible interaction between phosphate ions and concrete rebars due to hypothetic phosphate attack of reinforced concrete shall be considered, taking into account the reported occurrence of iron phosphate phases like vivianite ($Fe_3(PO_4)_2\cdot8(H_2O)$) and mitridatite ($Ca_2Fe_3(PO_4)_3O_2\cdot3(H_2O)$) under specific chemical–physical conditions [29].

### 1.2. Characteristics of the case study and aims of the research

The cementitious materials studied in this work were sampled from one of the dismissed structures of the Ex-Agrimont industrial facility, building C3, built in the 1950s near the coastline of Porto Marghera (Venice area, north-eastern Italy) (Fig. 1).

The Porto Marghera industrial area suffered from heavy pollution during the 20th century, due to uncontrolled emissions from chemical industries and oil refineries [30]. All production plants of the area were responsible for severe forms of atmosphere, water and soil pollution.

As for atmospheric emissions, a detailed monitoring during the years of maximum activity of the area is not available. Yet, an intensive monitoring campaign performed by the Regional Association for Environmental Protection (ARPA) during the years 1998–2004 [31], when most of the factories had already closed, still showed particularly severe atmospheric pollution from gaseous sulfur- and nitrogen-based pollutants, like hydrogen sulfide, sulfur dioxide and trioxide and ammonia.

Furthermore, during the years of maximum activity in the area, unauthorized dumps for the storage of toxic waste were frequently excavated, and by-product slurries and non-depurated process waters were dumped and dispersed with no control. All these activities contributed to the progressive pollution of the groundwater and soils of Porto Marghera with abnormal amounts of chlorinated and aromatic solvents, aromatic hydrocarbons, phenols, ammonia, aromatic amines, sulfates, phosphates, lead, cadmium, zinc, mercury and arsenic. The Ex-Agrimont area was particularly affected by soil and water pollution due to the leakage of process water from the industrial plant, which produced phosphate- and ammonia-based fertilizers by chemical extraction from insoluble minerals from 1927 until its closure in 1997.

The main sources of phosphate minerals are naturally-occurring sedimentary deposits of phosphorites, sedimentary rocks containing significant amounts (about 30%) of cryptocrystalline apatite. After the mining, phosphates are separated from accessory minerals (mainly clay minerals), and the concentrated material is then chemically processed to obtain phosphate-based fertilizers, mainly through what is known as the wet process method [32]. In this process, the phosphate raw materials react with sulfuric acid to produce phosphoric acid. More precisely, the reaction combines calcium from the phosphate with sulfate to form phosphoric acid and calcium sulfate, mainly gypsum (called phosphogypsum), according to the following simplified reaction:

$$Ca_5(PO_4)_3(OH, F, Cl) + 5H_2SO_4 + 10H_2O \rightarrow 3H_3PO_4 \qquad (1)$$
$$+ 5[CaSO_4 \cdot 2H_2O]\downarrow + H(OH, F, Cl)$$
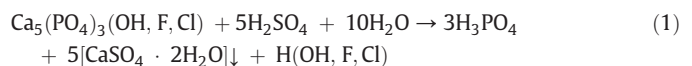
During the reaction, gypsum crystals precipitate and are separated from the acid by filtration and washing. Wet processed phosphoric acid normally contains 26 wt.% to 30 wt.% of P_2O_5, and depending on the types of fertilizer to be produced, it is usually concentrated from 40 wt.% to 55 wt.% of P_2O_5 through a series of vacuum evaporators, and subsequently, after reaction with ammonia, granulated to produce diammonium phosphate (DAP) and monoammonium phosphate (MAP). Granular triple superphosphate (GTSP), a non-nitrogen fertilizer, is produced by adding phosphoric acid to ground phosphate rock.

The production of fertilizers requires and produces a large volume of process water, a dilute mixture of phosphoric, sulfuric, and fluosilic acids with very low pH (about 1 to 2) [32]. Furthermore, it contains several other ions found in phosphate rock, as well as ammonia from the solid fertilizer-manufacturing process [32]. In order to reduce its environmental impact, process water commonly undergoes a series of chemical treatments, by sequential additions of calcium hydroxide and acids, to obtain a final solution with a pH of about 6.5 from which all solids and ammonia have been removed [32].

The studied structure (Fig. 1a) is a 20 m tall building, constituted by 22 couples of load-bearing reinforced concrete semi-arches. The structure is enclosed by a reinforced concrete wall up to 2 m high. Above this height the semi-arches are connected by prefabricated non-structural reinforced concrete beams which constituted the backing for the original fiber-cement roofing. A binder classifiable as CEM I-type cement (European Standard EN 197-1) was used for the manufacturing of all concrete elements, employing dosages between 300 and 350 kg/m^3 and with w/c ratios varying from 0.6 to 0.7. No chemical admixtures were added to the fresh mix. The aggregate fraction is characterized by

Fig. 1. a) Ex-Agrimont industrial plant, C3 building; b, c) concrete degradation on an arch in the south-western section of the structure.

a 20 mm maximum diameter and a granulometric distribution close to the theoretical Bolomey curve. The coarse aggregates consist mainly of carbonate rocks. Among the various carbonate species, sparry and micritic limestones and dolostones are dominant. The fine aggregate fraction consists of carbonate rock fragments of the same nature as the coarse aggregates and quartzite grains.

An intensive inspection survey highlighted the poor condition of the concrete structural frame of the building, despite the overall quality of the concrete and its good mechanical properties [33]. All structural elements are covered by superficial black crusts, which have caused dusting and superficial scaling of the cement matrix. The pervasive alteration caused, in some cases, complete consumption and detachment of concrete covers, triggering extensive oxidation on the underlying rebars. The weathering also affects the higher sections of the structure, indicating that atmospheric pollutants were responsible for the alteration of the concrete.

The degradation of reinforced concrete elements is further accentuated in the south-western section of the structure, near the platform originally used for the direct load of final products and by-products on trains. In this area, up until 2 m of height, the reinforced concrete of the arches and other structural elements is heavily scaled. The concrete cover is extensively detached showing pervasive oxidation of the rebars, and globular superficial concretions are present (Fig. 1b, c). Furthermore, the cementitious matrix is characterized by an anomalous white–yellowish color. It shows a relevant loss of cohesion, leading to pulverization in the worst cases.

Given the poor conditions of the C3 building and the heavy pollution affecting this area over the last few decades, the building has been thoroughly studied to verify the possible occurrence of a form of phosphate attack contributing to the decay of the concrete structural elements. More in detail, the objectives of the study are the following:

— To identify any possible interaction between saturating solutions rich in phosphate pollutants and reinforced concrete constituents (hardened cement paste, aggregate and steel rebars);

— To recognize the sequences of secondary phase crystallization;
— To verify the possible influence of pH gradients in the type and stability of secondary calcium phosphates crystallized within the altered materials;
— To verify the possible formation of gypsum–brushite solid solution phases within the altered materials due to the simultaneous occurrence of phosphate- and sulfate-based degrading agents, also considering a possible crystallization heterogeneity due to the presence of chemical gradients;
— To investigate the possible occurrence of secondary ammonium phosphates due to the interaction between phosphate- and nitrogen-based pollutants and concrete;
— To study the interaction between phosphate pollutants and steel rebars;
— To improve the knowledge on the dehydration behavior of the gypsum–brushite solid solution under temperature regimes compatible with the ones acting on concrete structures in temperate climates, also taking into account for possible crystal size and kinetic factors on the thermal stability of the compounds;
— To elaborate a qualitative model for the evolution of the degradation, verifying it through simple thermodynamic calculations.

2. Materials and methods

2.1. Materials

Due to the considerable lack of coherence of the materials, samples were mechanically separated from the substrate with a metal chisel and superficial concretions were collected with a scalpel. Nine samples of altered concrete were taken from different structural elements of the building, below 2 m of height, where the superficial scaling is more pervasive (Fig. 2): 3 from adjacent arches (B2A1, B2A2, B2A3), 3 from the outer walls of the structure (B2M1, B2M2, B2M3) and 3 from the railway platform (B2B1, B2B2, B2B3). In addition, 3 fragments of superficial

concretions (B2E1, B2E2, B2E3) were sampled from areas adjacent to B2A1, B2M1 and B2B1 sampling points.

The altered concrete samples were impregnated with epoxy resin and cross-cuts were thin sectioned. The macroscopic structure in cross section is similar for all samples, showing a marked textural stratification of the altered cement matrices (Fig. 3a, b). Five different alteration layers, characterized by typical chromatic and morphological features, may be recognized from the external surface to the core of the samples (Fig. 3b):

— An external superficial concretion (denominated L1) of dusty white–grayish material, characterized by irregular shapes and a thickness generally between 100 and 800 μm;
— A continuous black crust (denominated L2) underneath the L1 layer, more compact than the superficial concretion and characterized by a thickness generally between 200 and 500 μm;
— A continuous layer of altered cementitious matrix (denominated L3) underneath the black crust, characterized by an anomalous gray–yellowish color, low cohesion and a thickness between 1.5 and 2.5 mm;
— An irregular layer of altered cementitious matrix (denominated L4) underneath the L3 layer, characterized by an anomalous white–grayish color, low cohesion and a thickness generally between 1 and 3 mm;
— A thick layer of altered cementitious matrix (denominated L5) underneath the L4 layer, characterized by an anomalous gray–yellowish color, low cohesion and a thickness generally between 1 and 3 cm.

Due to the reduced thickness of the concrete cover, the rebars are generally located within the L5 alteration layer, and they are characterized by marked macroscopic oxidation features, like typical red–brownish colors testifying the development of rust from the pristine steel, severe loss of cross section and irregular profiles (Fig. 3a). In the worst cases, a considerable amount of rust accumulates around the altered rebars, and permeates the surrounding cementitious matrices. Only small and isolated areas within the sampled materials retain the structure of unaltered cementitious materials.

2.2. Methods

The analytical campaign was divided in two distinct phases, preparatory to the formulation of a complete alteration model. The first phase was aimed at performing a thorough micro-mineralogical, micro-chemical and micro-structural characterization of the altered concrete materials sampled from the studied structure. The second phase was aimed at performing a detailed experimental study of the dehydration
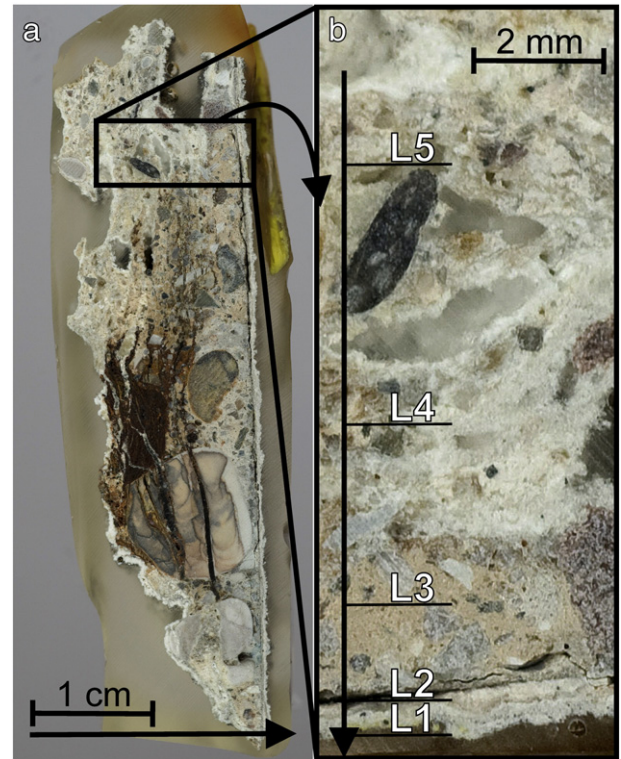
Fig. 3. a) Typical textural aspect of the altered concrete samples in cross section (sample B2A1). The arrow is pointed from the core to the external surface of the altered conglomerate. The cross section of an altered rebar is visible (red–brownish area toward the center of the sample); b) magnification of the area highlighted by the rectangle in Fig. 3a. The arrow is pointed from the core to the external surface of the sample, and the five typical alteration layers are indicated by lines.

behavior of the gypsum–brushite solid solution, to better understand the occurrence of partially and totally dehydrated secondary sulfate and phosphate phases within the altered samples and to correlate such evidences with the seasonal temperature variations acting on concrete structures placed in temperate climates.

As for the characterization of the altered materials, all thin sections were studied by means of a polarizing light microscope to carry out a preliminary morphological study of secondary phases. Explorative
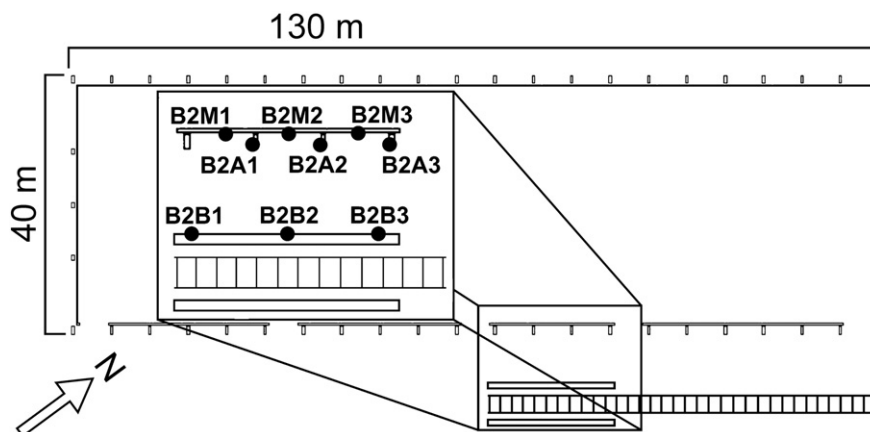
Fig. 2. Sketch of the productive plant, indicating the area from which the samples studied in this research were collected.

bulk X-ray powder diffraction (XRPD) analyses were performed according to the acquisition procedure 1 (Table 1) on the grain size fraction under 63 μm of the samples, obtained by dry disaggregation and sieving. The diffraction patterns acquired during the study, also using different acquisition procedures, were all interpreted with X'PertHighScore Plus 3.0 software by PANalytical. The mineral profiles of the compounds were reconstructed by comparing the reflection positions of the detected diffraction patterns with entries of ICDD (International Center for Diffraction Data) and ICSD (Inorganic Crystal Structure Database) databases.

In addition to the bulk XRPD study, a detailed mineralogical profile analysis was carried out to reconstruct the secondary phases' stratigraphy. A number of localized profile micro-samplings were performed on the altered paste of the samples with a MicroMill® high precision microsampling device developed by New Wave Research. Materials were sampled along 50 μm thick paths, parallel to the external surface, at a distance of about 200 μm from each other. XRPD analyses were then performed according to procedure 1 (Table 1), and diffraction patterns were acquired on a silicon zero-background.

To verify the mineralogical profile, synchrotron-based micro-diffraction analyses were performed on two samples (B2A1, B2B2). After consolidation by vacuum impregnation with epoxy resin, the samples were cut transversally, mounted on 300 μm thick Plexiglas foils and reduced to a thickness of 100 μm. Measurements were performed at the μ-spot beamline of BESSY II third generation synchrotron radiation facility in Berlin [34,35], according to the acquisition procedure 2 (Table 1).

In addition to point analyses, a series of linear scans were performed parallel to the reaction fronts, in aggregate-free areas, with a spatial resolution of 30 μm, which significantly increased the count statistics.

Microchemical and microstructural analyses on both thin sections and massive samples were carried out using a Camscan MX 2500 scanning electron microscope (SEM), equipped with a LaB_6 electron source and an EDAX energy dispersive X-ray detector (EDS). Qualitative interpretation of spectra and semiquantitative analysis of chemical profiles were performed through SEMQuantPhizaf software. Furthermore, EDS chemical maps were acquired and elaborated through a multi-elemental image analysis procedure, modified after Stutzman [36] for quantitative image analysis of ordinary Portland cement. Quantitative mineralogical maps were obtained for the interface areas between oxidized rebars and the surrounding altered cement matrix. Before performing image analysis, all the acquired maps underwent an enhancement procedure through ImageJ software, consisting of an optimization of the brightness/contrast values and in the removal of background noise artifacts, applying a 0.2 pixel radius median filter. Then, chemical maps and their corresponding BSE image were merged through ENVI 4.7 software, obtaining a 12-band composite image. The discrimination of mineral phases was based on the creation of composite RGB images constituted by three maps of the main chemical constituents of the minerals. Combining such maps, each mineral constituent of the analyzed area was defined by a class described with an adequate number of training pixels. The multi-band images were classified through a maximum likelihood algorithm, obtaining a mineralogical map of the analyzed areas.

As for the study of the dehydration behavior of the secondary phases, the first step was the synthesis of the two end members of the gypsum–brushite solid solution and two homogeneous intermediate solid solution phases, by gradually adding an $(x)M\ Na_2SO_4 + (0.5-x)$ $M\ NaH_2PO_4 \cdot H_2O$ aqueous solution to a 0.5 M $CaCl_2$ aqueous solution. At each synthesis, the (x) term was varied between 0 and 0.5 in order to change the relative proportions of the end members. All the syntheses were performed at 25 °C, maintaining the solution at pH = 5 by gradual addition of NaOH.

The phases were analyzed by XRPD, according to procedure 3 (Table 1). Structural refinements of the synthesized compounds were performed through full-profile fitting according to Rietveld method [37], using TOPAS software by Bruker AXS.

The quantitative determination of Ca, S and P concentrations on the phases were determined by inductively coupled plasma optical emission spectrometry (ICP-OES) using a Thermo Scientific iCAP 6200 spectrophotometer. The concentration limit and analytical accuracy of the determined elements are lower than 1 ppb and within 2% relative, respectively.

A qualitative estimation of crystal sizes of the synthesized compounds was performed through SEM imaging.

The dehydration behavior of the compounds was studied by simultaneous thermogravimetric analyses (TGA) and differential thermal analyses (DTA), performed using a NETZSCH STA 409 PC Luxx thermal analyzer, with a heating rate of 10 °C/min (from 20 to 1000 °C) in flowing air (flow rate: 20 ml/min).

Mineralogical evolution of the phases during heating were studied by in situ XRPD using an Anton Paar HTK 16 High-Temperature Chamber working with a Platinum heating filament, according to the acquisition procedure 4 (Table 1). Multiple diffraction patterns were acquired in the 20 °C–300 °C temperature interval, with 10 °C/min and 4 min as heating rate and soaking time at the target temperature, respectively.

To consider the reaction kinetics of the dehydration of the phases, the compounds were thermally treated at 80 °C for 48 h. Mineralogical profiles of the materials were determined by XRPD, according to procedure 3 (Table 1). Semiquantitative analyses were performed by full profile analysis following the Rietveld method [37], using X'PertHighScore Plus 3.0 software by PANalytical. The starting models for the structure refinement were selected from the ICSD.

In order to evaluate the influence of crystal size on the dehydration kinetics of the phases, the synthesized materials were ground with a Retsch Mixer Mill MM200 (60 min, 50 Hz frequency). After a check of the crystal size reduction both by SEM imaging and XRPD, the samples were thermally treated at 80 °C for 48 h and analyzed by XRPD, with

Table 1

Instrumental settings for the different XRD measurements performed on the studied samples. Different acquisition settings for synthesized samples and thermally treated synthesized samples are distinguished in procedure 3 with * and **, respectively.

	Procedure 1	Procedure 2	Procedure 3	Procedure 4
Instrument	Philips X'Pert	μ-spot beamline	PANalytical X'PERT PRO MPD	Philips X'Pert
Geometry	Bragg–Brentano	Transmission	Focalising transmission	Bragg–Brentano
Detector	X'Celerator	MarMosaic 225 2-D (3072 × 3072 pixels)	PIXcel	X'Celerator
Sample support	Aluminum plate or silicon zero-background	Plexiglas foil	Boron–silicate glass capillary (200 μm diameter)	Platinum sample holder
Radiation	CuKα	Synchrotron light	CuKα	CuKα
Wavelength	1.5406 Å (Kα1)	1.0656 Å	1.5406 Å (Kα1)	1.5406 Å (Kα1)
Radiation spot size		30–250 μm		
Scan Axis	θ-2θ vertical goniometer	Transmission geometry	θ-θ vertical goniometer	θ-2θ vertical goniometer
Start-end positions ° [2θ]	3–80	3–75	* 5–105 ** 3–70	10–54
Acquisition rate ° [2θ]/s	0.02		* 0.013 ** 0.026	0.033
Scan type	Continuous	Continuous	Continuous	Continuous
Instrument settings	40 kV–40 mA	15 keV	40 kV–40 mA	40 kV–40 mA

the same instrument and operating conditions used for the kinetics studies (procedure 4, Table 1). Finally, the dehydration behavior of the ardealite-like phase was studied at high temperatures. The sample materials were thermally treated in a muffle at 400 °C and 550 °C for 4 h, followed by a phase analysis by XRPD.

3. Results

3.1. Characterization of the altered materials

The diffraction patterns of the finer fraction of the altered concrete samples revealed a complex mineral assemblage. Besides the occurrence of aggregate-related phases (quartz, calcite, dolomite, plagioclase, biotite and chlorite), peaks of secondary sulfate and phosphate phases were detected (Fig. 4). More specifically, apatite, associated with gypsum and brushite in solid solution, octacalcium phosphate, a mineral phase with crystal structure similar to ardealite and struvite were observed in the samples. The absence of portlandite peaks testifies the almost total decalcification of the cementitious matrix.

Apatite reflections are characterized by high full width at half maximum (FWHM) values, indicating a low crystallinity of the phase. The displacements in reference [2θ] values of both gypsum and brushite reflexes indicate that gypsum and brushite occur as solid solution. Furthermore, remarkable displacements in reference [2θ] values of ardealite peaks suggest the occurrence of mineral phases with an ardealite-like structure, presenting SO_4/HPO_4 ratios close to the stoichiometric value.

The profile diffraction analyses clearly show a mineralogical zoning through the samples: the L1 layers (Fig. 5a) are mainly constituted by gypsum–brushite solid solution and ardealite-like phases, associated with β-anhydrite and bassanite. The L2 layers (Fig. 5b) are mainly formed of monetite ($Ca(HPO_4)$), an anhydrous calcium hydrogen phosphate that forms after the dehydration of brushite. Octacalcium phosphate, apatite and gypsum–brushite solid solution are also present. L3 layers (Fig. 5c) are characterized by a drastic decrease in monetite content, associated with an increase of gypsum–brushite solid solution and ardealite-like phases and a less marked increase in octacalcium phosphate and apatite content. Moving toward the core of the samples (Fig. 5d), L4 layers are characterized by the almost complete disappearance of gypsum–brushite solid solution, and a relevant increase in octacalcium phosphate content. Finally, octacalcium phosphate is completely replaced by apatite in L5 layers (Fig. 5e), where it represents the only Ca-containing phase. Ammonium–magnesium phosphates, also in monohydrate form, corresponding to the mineral dittmarite, were also detected in L4 and L5 layers.

A relative estimate of apatite crystallinity was performed considering the FWHM of (002) plane diffraction peak of 15 diffraction patterns, selected among those without a peak overlap with other phases. More in detail, five diffraction patterns were selected among those related to L2 and L3 layers, where monetite and gypsum–brushite solid solution are the dominant phases, five from the L4 layer where octacalcium phosphate is the dominant phase, and five from the L5 layer, where apatite is the dominant phase. A clear increase in FWHM values can be observed moving toward the inner layers of the samples (Table 2), indicating a progressive decrease in apatite crystallinity. FWHM values of apatite of the L4 layer are quite disperse (high standard deviation), so that two groups can be identified: one with values corresponding to those observed on apatite of the outermost layers, and another with values similar to those relative to the L5 layer.

The micro-diffractions of the altered rebars, at the interface with the surrounding matrix, indicate a mineralogical assemblage exclusively constituted by iron oxides (magnetite(Fe_3O_4)) and oxyhydroxides (goethite FeO(OH), and lepidocrocite γ-FeO(OH)), confirming the high degree of oxidation of the reinforcements (Fig. 5f). No traces of iron phosphates, like vivianite ($Fe_3(PO_4)_2 \cdot 8(H_2O)$) and mitridatite ($Ca_2Fe_3(PO_4)_3O_2 \cdot 3(H_2O)$), were found.

Microstructural and microchemical analyses confirm the strong decalcification of the cement matrices and a relevant occurrence of alteration processes also on the carbonate aggregate fraction. SEM imaging and profile microanalyses on the cement matrices (Fig. 6a) indicate a progressive increase of calcium and phosphorous content toward the pore network of the materials, often completely filled by secondary phases, while the cores of the hardened pastes are significantly depleted in calcium and enriched in silicon. Such micro-structural and microchemical features indicate a marked leaching of calcium from the cement matrices, with formation of secondary calcium phosphates toward the pore network of the altered concretes. Carbonate aggregates are also severely decalcified, showing frequent dissolution rims at the interface with the surrounding matrix (Fig. 6b).

The profile microstructural analyses on fresh-cut surfaces at different depths provided information on the crystallization sites, morphological features and composition of the secondary phases. L1 layers are constituted by well-formed euhedral bassanite and β-anhydrite crystals, surrounded by a matrix of microcrystalline tabular crystals of gypsum–brushite solid solution (Fig. 7a). L2 layers are formed by dense clusters of tabular monetite crystals (Fig. 7b), and cryptocrystalline
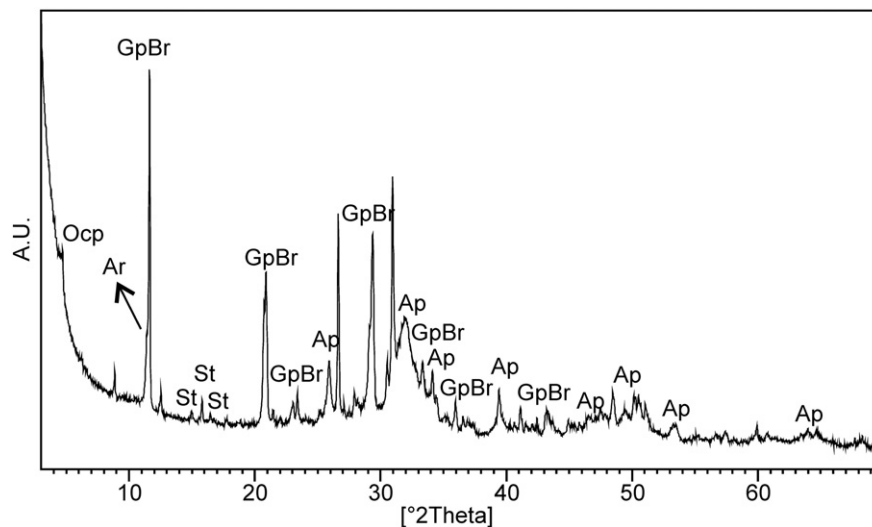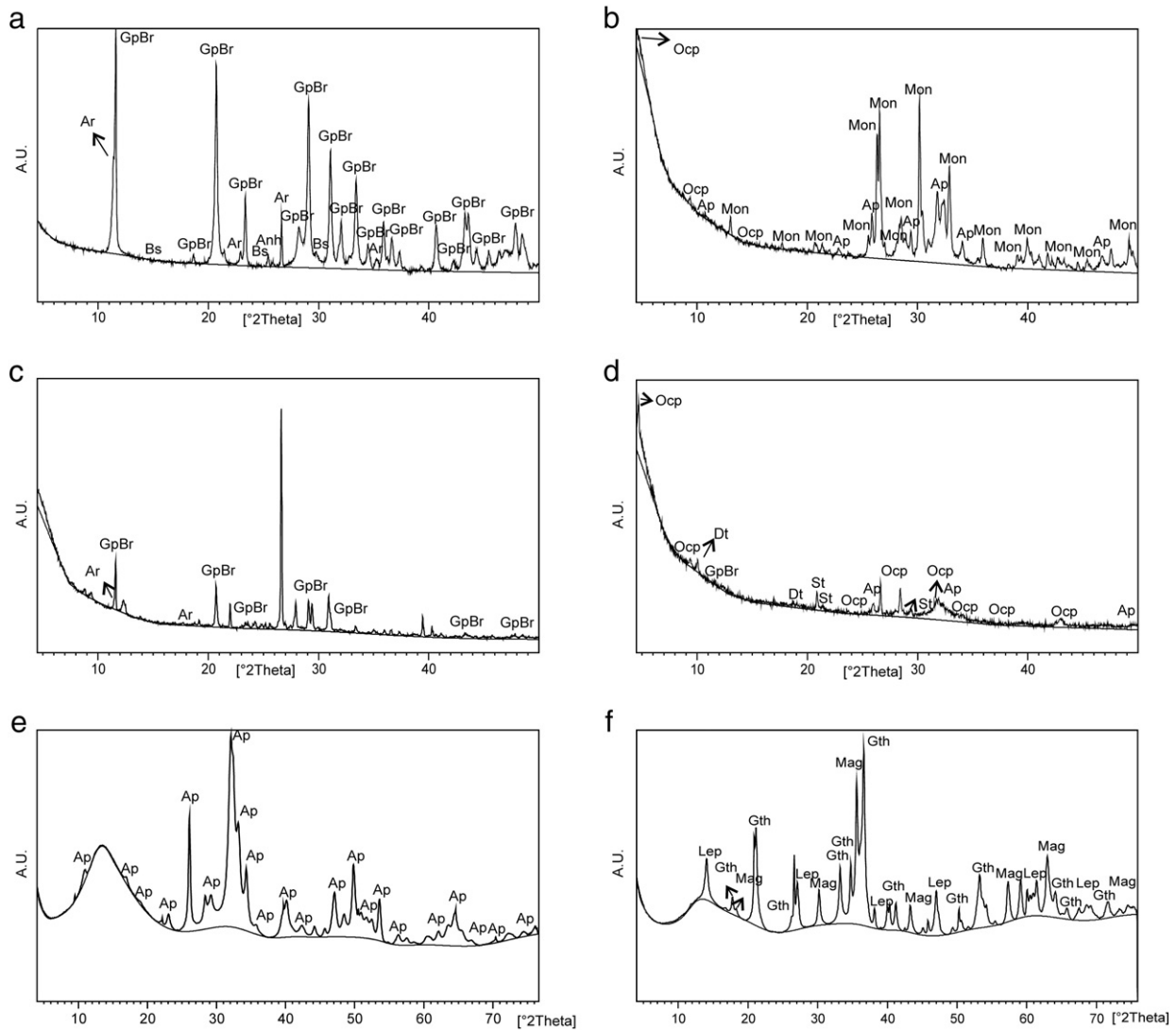

Fig. 4. Typical diffraction pattern of the finer fraction of the altered concrete (sample B2B1). Main peaks of the secondary mineralogical phases are indicated. Abbreviations: Ap = apatite, Ar = ardealite-like phase, GpBr = gypsum-brushite solid solution, Ocp = octacalcium phosphate, St = struvite.

Fig. 5. Typical micro-diffraction patterns of the concrete matrix within the defined alteration layers (sample B2A1): a) L1 layer; b) L2 layer; c) L3 layer; d) L4 layer; e) L5 layer; f) altered rebar, at the interface with the surrounding matrix. The main peaks of the secondary mineralogical phases are indicated. Abbreviations: Anh = β-anhydrite, Ap = apatite, Ar = ardealite-like phase, Bs = bassanite, Dt = dittmarite, GpBr = gypsum–brushite solid solution, Gth = goethite, Lep = lepidocrocite, Mag = maghemite, Mon = monetite, Ocp = octacalcium phosphate, St = struvite.

clusters of apatite grown epitaxially on monetite seed crystals. L3 layers are constituted mainly by microcrystalline clusters of tabular gypsum–brushite solid solution phases (Fig. 7c). Recurrent epitaxial growth of cryptocrystalline apatite on gypsum–brushite solid solution seed crystals was also observed (Fig. 7d).

The chemical composition of the gypsum–brushite solid solution in the L1 layers is very homogeneous (standard deviation of SO_4^{2-}/HPO_4^{2-} molar ratio: 0.18), with the prevalence of ardealite-like phases (mean SO_4^{2-}/HPO_4^{2-} molar ratio of 1.23), whereas that of the L2 and L3 layers

is more variable (standard deviation of SO_4^{2-}/HPO_4^{2-} molar ratio: 0.53), with a mean value of 1.15 and general prevalence of gypsum-rich phases.

The L4 layers are mainly constituted by strongly pinacoidal octacalcium phosphate crystals, often forming fan-shaped structures, with associated large subhedral and euhedral struvite and dittmarite crystals (Fig. 7e). Cryptocrystalline apatite clusters are also observable.

Finally, L5 are constituted by clusters of cryptocrystalline apatite, characterized by globular and platy morphologies, and well-formed euhedral struvite and dittmarite crystals (Fig. 7f).

Both apatite and ammonium–magnesium phosphates are characterized by limited isomorphic substitutions. More specifically, apatite has a mean PO_4^{3-}/SO_4^{2-} ratio of 19.4 with relatively low standard deviation (3.4) and mean Cl^- molar concentrations of 0.65% over the total mass of the materials (standard deviation: 0.16). Ammonium–magnesium phosphates are characterized by a scarce NH_4^+–K^+ substitution, with mean K^+ molar concentrations of 0.84% over the total mass (standard deviation: 0.63).

The quantitative image analysis (Fig. 8), performed at the interface between oxidized rebars and the altered matrix, confirmed the diffuse oxidation of the rebars and the lack of any iron phosphates, like vivianite

Table 2
Mean FWHM values and relative standard deviation of HAP (002) planes diffraction peaks according to the dominant phase of the diffraction pattern. Abbreviations: Ap = apatite, GpBr = gypsum–brushite solid solution, Mon = monetite, Ocp = octacalcium phosphate.

Layer	Dominant phase	Mean FWHM of HAP (002) peak	Standard deviation
L2, L3	Mon, GpBr	0.185	0.019
L4	Ocp	0.217	0.042
L5	Ap	0.318	0.026
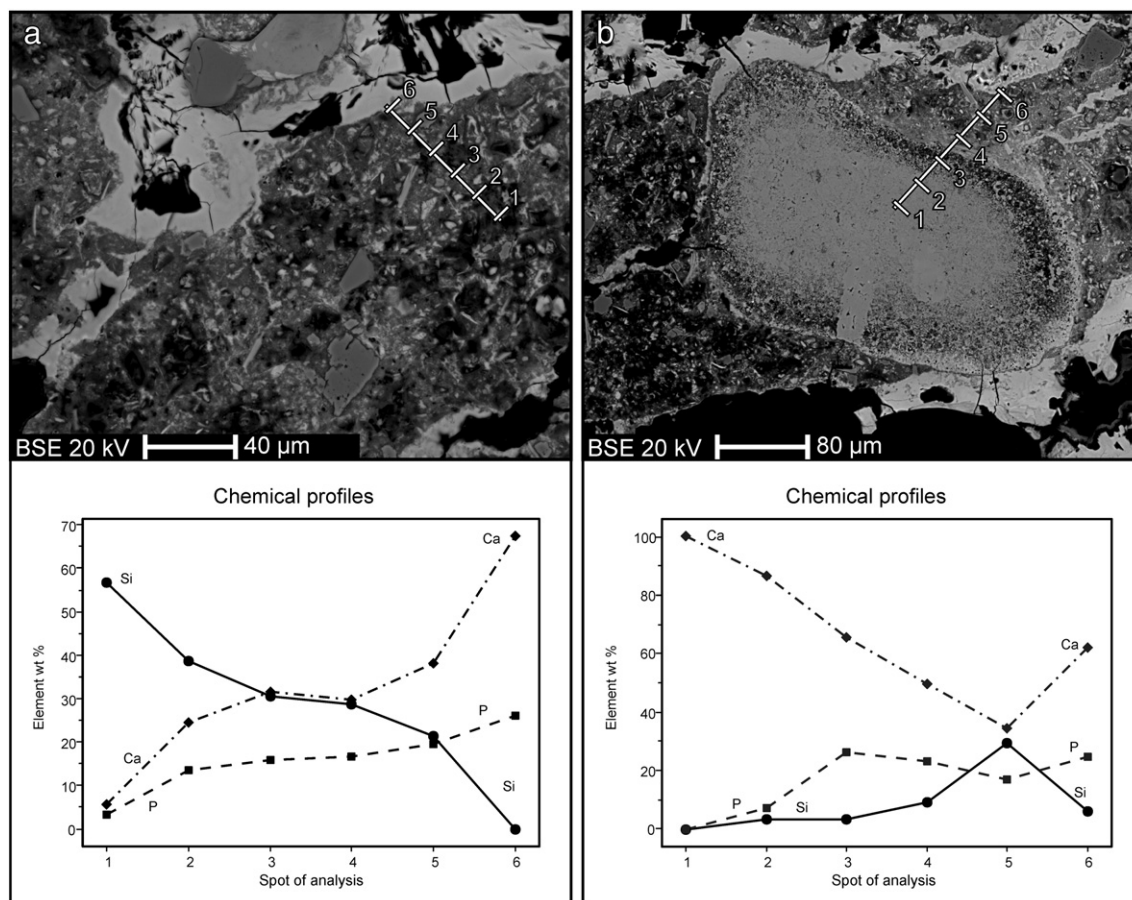
Fig. 6. a) Typical backscattered electron (BSE) image of an area of decalcified cement matrix (sample B2A2, layer L5) and chemical profile of Si, P and Ca of the six points of analysis indicated in the image; b) bypical BSE image of an altered carbonate aggregate (sample B2A2, layer L5) and chemical profile of Si, P and Ca of the six points of analysis indicated in the image.

and mitridatite. Furthermore, iron chlorides within the altered rebars may be observed. Gypsum–brushite solid solution phases are present in contact with iron hydroxide, while in the internal layers apatite and octacalcium phosphate are detected.

3.2. Dehydration behavior of secondary phases

The dehydration behavior of the gypsum–brushite solid solution was studied on four synthesized compounds: the two end-members of the solid solution, and on two intermediate phases, one close to the brushite end-member (hereinafter referred to as brushite-near) and the other close to the stoichiometric compound ardealite (hereinafter referred to as ardealite-like). XRPD analyses indicated that all four synthesized compounds were pure. Gypsum, brushite and brushite-near structures were determined by Rietveld refinement. For the ardealite-like phase, a structural refinement was not possible, and a Le Bail fit was performed instead. Calculated unit cell parameters for the four phases are reported in Table 3, together with the SO_4^{2-}/HPO_4^{2-} molar ratio determined by ICP-OES.

The four phases, despite being quite polydisperse, are characterized by heterogeneous crystal sizes. The end-members are characterized by a good degree of crystallinity, being constituted by tabular crystals with an average size of around 20–30 μm (Fig. 9a, b). The crystallinity decreases moving toward the stoichiometric compound of the solid solution: the brushite-near phase is constituted by crystals with an average size of 7–10 μm (Fig. 9c), which decreases to around 2–4 μm for the ardealite-like phase, with a significant occurrence of clusters of cryptocrystalline particles (Fig. 9d).

Although both gypsum and brushite are characterized by a 21–22% weight loss in the temperature range 100–220 °C, corresponding to

the loss of structural water, the dehydration process is significantly different for the two phases (Fig. 10a, c). The dehydration of gypsum involves an initial loss of about 75% of the water molecules and the formation of bassanite in the temperature interval comprised between 110 °C and 155 °C, as indicated by a marked exothermic peak in the DTA curve at 155 °C. The complete dehydration of the phase and the formation of anhydrite occur between 170 °C and 200 °C, as indicated by a DTG peak at 177 °C and by a shoulder in the main exothermic peak of the DTA curve, centered at about 190 °C (Fig. 10a). These results are consistent with those in the literature [38].

Brushite dehydrates to form monetite in two subsequent steps, one in the thermal interval between 110 °C and 190 °C, with a 5.13% weight loss, and a second, more significant, between 190 °C and 200 °C (Fig. 10c). This two-step process, apparently in contrast with literature data [39], may be related to the dehydration at lower temperatures of that fraction of material with lower crystallinity. The phase underwent a further weight loss in the temperature range between 400 °C and 450 °C, probably related to the deprotonation of HPO_4^{2-} groups and the formation of calcium pyrophosphate ($Ca_2P_2O_7$).

In situ XRPD analysis of the two end-members provided results in line with those observed by thermal analyses. Gypsum partially dehydrates to form bassanite in a temperature interval between 110 °C and 140 °C, while total dehydration occurs in the interval between 190 °C and 220 °C, to form γ-anhydrite (Fig. 10b). As for brushite, a first limited dehydration of the cryptocrystalline fraction of the material occurs in the temperature interval between 120 °C and 130 °C, while the main dehydration event occurs between 180 °C and 190 °C, where the total conversion into monetite occurs (Fig. 10d).

The thermal behavior of the brushite-near phase is similar to the one of the brushite end-member, with the exception that the weight loss
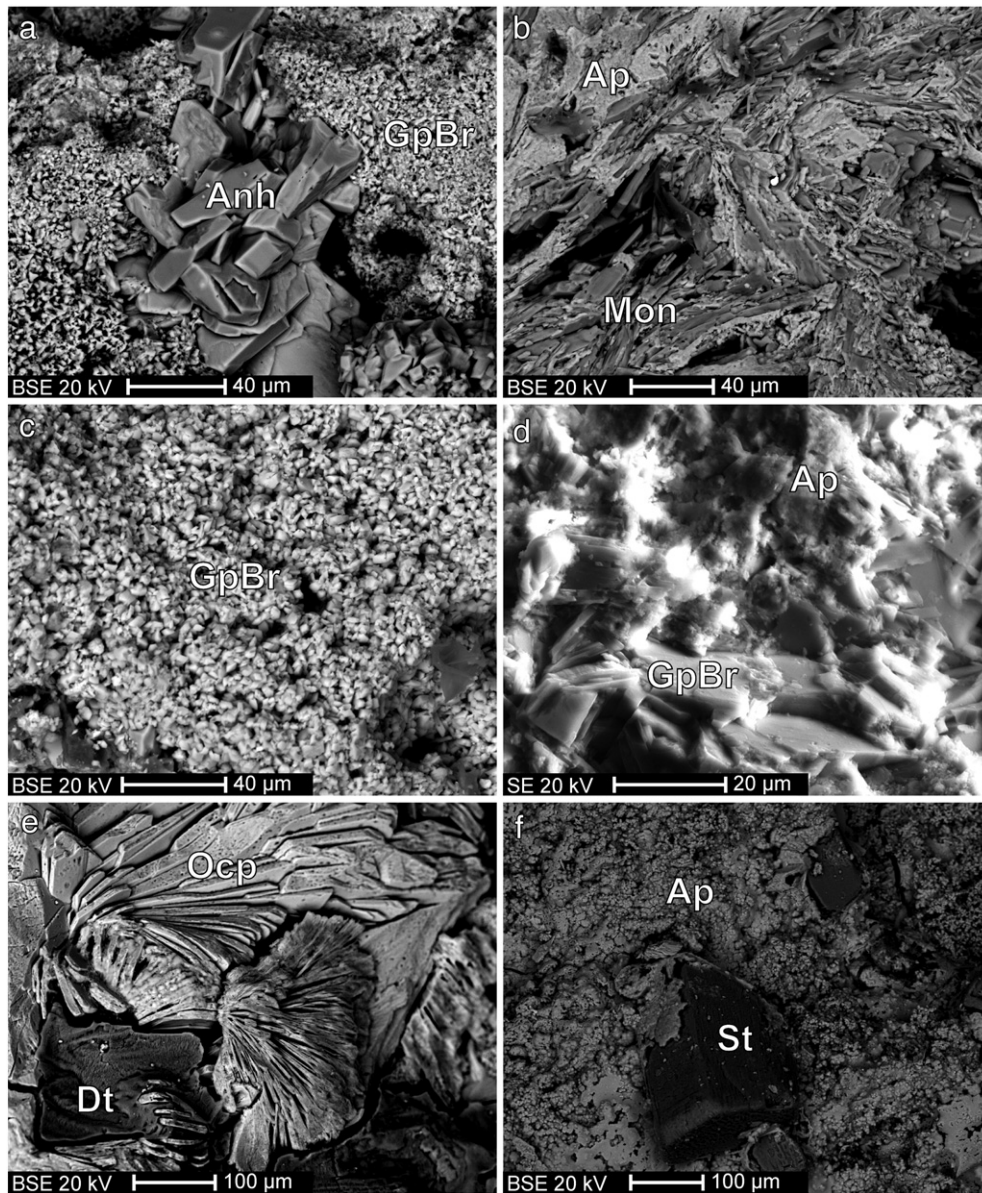
Fig. 7. Typical profile SEM analyses (sample B2A3): a) L1 layer, BSE image of β-anhydrite crystals in a matrix of microcrystalline gypsum–brushite solid solution; b) L2 layer, BSE image of monetite crystals with apatite grown epitaxially (the latter appears whiter); c) L3 layer, BSE image of microcrystalline gypsum–brushite solid solution clusters; d) L3 layer, secondary electrons (SE) image showing epitaxial growth of apatite on gypsum–brushite solid solution crystals; e) L4 layer, BSE image of fan-shaped octacalcium phosphate clusters, with associated ammonium magnesium phosphate crystals (the latter appears darker); f) L5 layer, BSE image of euhedral ammonium–magnesium phosphates in a matrix of cryptocrystalline apatite. Abbreviations: Anh = β-anhydrite, Ap = apatite, Dt = dittmarite, GpBr = gypsum–brushite solid solution, Mon = monetite, Ocp = octacalcium phosphate, St = struvite.

between 100 °C and 190 °C is half that of the pure end-member, despite the lower crystallinity of the solid solution (Fig. 10e). Moreover, the main weight loss occurs at temperatures slightly higher than that of the end-member (DTG peak at 197 °C, exothermic DTA peak at 205 °C). Generally, this phase shows better thermal stability compared to the pure end-member.

In situ XRPD shows that the brushite-near phase dehydrates to form monetite in a single temperature interval, between 180 °C and 210 °C (Fig. 10f). The formation of anhydrous calcium sulfates due to the separation of sulfate and phosphate phases from the solid solution was not observed. This is probably due to the poor detection limits of the in situ XRPD analysis, and the low amounts of calcium sulfates of a brushite-near solid solution. These analytical results confirm the higher thermal stability of the solid solution with respect to the pure phosphate end-member.

The thermal behavior of the ardealite-like phase is significantly different from that of the other synthesized compounds (Fig. 10g),

since this phase has a weight loss between 100 °C and 220 °C lower (18.52%) than that observed for the other phases. The main dehydration event led to the formation of γ-anhydrite with an extremely low degree of crystallinity, as deduced by the few low-intensity peaks in the diffraction pattern (Fig. 10h); furthermore, a remarkable displacement in reference [2θ] values with respect to typical γ-anhydrite can be observed, probably due to the SO_4^{2-}–HPO_4^{2-} isomorphic substitution in the crystal structure of the phase. A subsequent gradual weight decrement of 2.54% in the 200 °C–400 °C temperature range can be related to a continuous loss of the remaining structural water, which did not evaporate in the main dehydration event. A third significant weight loss is then observable between 850 °C and 1000 °C, probably in relation to the HPO_4^{2-} groups deprotonation and the formation of calcium pyrophosphate. The analytical results confirm a better thermal stability of this term of the solid solution with respect to the other phases, and indicate the lack of separation of the solid solution in the investigated temperature interval, with formation of an anhydrous solid solution phase.
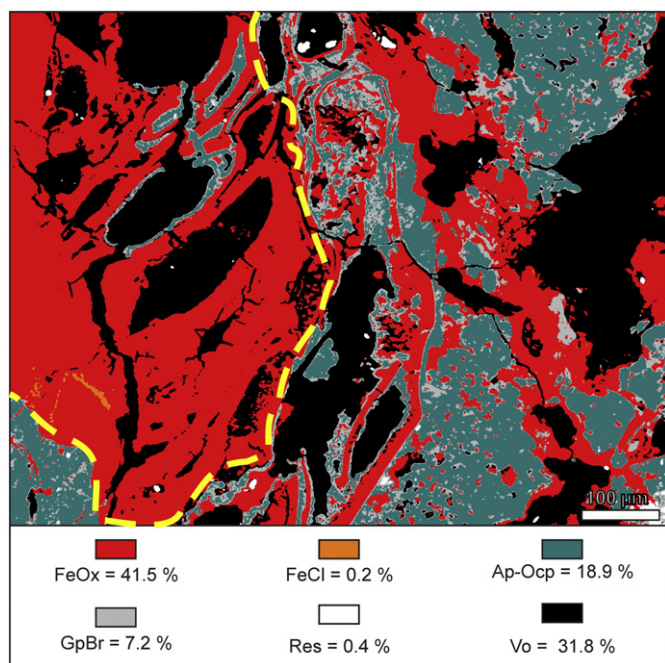
Fig. 8. Typical mineralogical map of the altered rebars – matrix interface area (interface line highlighted by the yellow dashed line) and volumetric estimate of phases (sample B2M2, L5 layer). Abbreviations: Ap–Ocp = apatite and octacalcium phosphate, FeCl = iron chlorides, FeOx = iron oxides–hydroxides, GpBr = gypsum–brushite solid solution, Res = residual unaltered cementitious matrix, Vo = voids.

The gypsum end-member underwent significant dehydration after thermal treatment at 80 °C for 48 h, with the formation of a mixture of bassanite (71.9%) and gypsum (28.1%)(Fig. 11a, Table 4). Compared to those determined during the in situ XRPD analyses, the lower dehydration temperature hereby observed, indicates a strong influence of kinetics for the triggering of the process. The brushite end-member underwent limited dehydration (3.6% of monetite formation), probably involving the less crystalline fraction only (Fig. 11b, Table 4). Solid solution phases did not undergo dehydration (Fig. 11c, d, Table 4), confirming a better thermal stability with respect to the end-members.

The grinding process was effective in the reduction of the crystal size of the phases, as confirmed both by XRPD data (dramatic increase in FWHM of the diffraction peaks) and SEM imaging. The crystal size reduction, with a consequent increase in the defectivity of crystals, caused significant changes in the thermal behavior of the synthesized phases, with an overall increase in the dehydration rate of the compounds during the 48-h thermal treatment. Thus, the combination of crystal size and kinetic factors resulted to be fundamental for the stability of hydrated phases at temperatures below 100 °C. The gypsum end-member underwent massive dehydration, with the formation of a compound constituted by 97.3% bassanite and 2.7% β-anhydrite (Fig. 11a, Table 4). No traces of hydrated phases were found. The dehydration of the brushite end-member increased significantly, with the formation of a compound constituted by 62.5% monetite and 37.5% brushite (Fig. 11b, Table 4).

Table 3
Unit cell parameters and SO_4^{2-}/HPO_4^{2-} molar ratios of the synthesized phases.

Phase	a (Å)	b (Å)	c (Å)	β	SO_4^{2-}/HPO_4^{2-} molar ratio
Gypsum	5.6866	15.2301	6.5365	118.4855	676.183
Brushite	5.8110	15.1800	6.2389	116.3902	0.004
Brushite-near	5.8075	15.1831	6.2500	116.4323	0.054
Ardealite-like	5.682	31.063	6.345	117.40	0.828

The thermal behavior of solid solution compounds was affected by the grinding process, but their thermal stability was better than that of the end-members. The brushite-near phase underwent a significant dehydration process, which left only 29.9% of the original phase, and produced a dehydrated fraction formed by monetite (69.6%) and bassanite (0.5%) (Fig. 11c, Table 4) with a net separation of the sulfate and phosphate phases from the solid solution, to form separate dehydration products.

The ardealite-like phase underwent partial dehydration, with formation of SO_4^{2-}–HPO_4^{2-}-substituted γ-anhydrite (Fig. 11d, Table 4). In this case, the solid solution did not separate. Unlike the previous case, the separation of the sulfate and phosphate phases occurred only at high temperatures, with the formation of SO_4^{2-}–HPO_4^{2-}-substituted γ-anhydrite, associated with pure β-anhydrite and monetite (Fig. 12). The absence of hydrated phases indicates that the compound dehydrated completely.

The experimental treatments of the different synthesized compounds clearly indicate that the ardealite-like phase has a better thermal stability than the other solid solution phases.

4. Discussion

On the basis of the analytical results, a qualitative model, based on four main phases, is hereby proposed to describe the alteration processes occurring in the studied concrete.

The results of the previous analyses performed on unaltered portions of the concrete structure [33] suggest that the cementitious matrix of the degraded conglomerate was constituted mainly by C–S–H and CH, and the alkaline environment of the conglomerate ensured the permanence of a passivation layer around the rebars. The chemical nature of the secondary phases detected in the analyzed samples leads to hypothesize a process of saturation of the concrete pore network by capillary suction of a solution of process water and saltwater, under the action of environmental pollutants (Fig. 13a). The typical composition of process waters from the production of phosphate-based fertilizers [32], the mean salinity and composition of Venice lagoon brackish waters [40] and a hypothetical 1 to 1 ratio between the two components, indicate that the saturating solution was particularly rich in phosphates, sulfates, chloride and ammonia, with values above 3000 mg/l for the first two types of chemical compounds, and above 1000 mg/l for the last ones. Furthermore, a local enrichment in dissolved sulfate species in the pore solution saturating the external layers of the materials may be assumed, due to the gas liquid absorption of sulfur-based atmospheric pollutants. This process led to a stronger acidification of the external layers, while the pH drop was titrated in the cores by the basic environment. All these factors caused significant mineralogical changes in the cementitious matrix. C–S–H, CH and carbonate minerals constituting the aggregate fraction (calcite and dolomite) underwent dissolution and/or decalcification, and secondary phases precipitated upon reaching supersaturation conditions. The nature of the secondary phases was strongly controlled by pH and sulfate gradients, causing heterogeneous precipitation in the different layers (Fig. 13b). More in detail, acidic precursors of apatite, such as brushite [17], formed in the external layers (L1, L2 and L3), in solid solution with gypsum. A high chemical variability of the solid solution phases was detected, with a general prevalence of gypsum-rich phases. These phases formed in proximity of the rebars, too, where a local acidification was promoted by chloride attack [41, 42]. The absence of iron phosphates at the interface between altered rebars and surrounding matrix is related to highly acidic conditions, which inhibited their precipitation, favored by higher pH instead [29]. Moving toward the inner layers, increasingly basic apatite precursors – octacalcium phosphate [16] and amorphous calcium phosphate [17] – formed once their typical pH stability fields were reached. In particular, octacalcium phosphate precipitated in the L4 layers and amorphous calcium phosphate precipitated in the L5 layers. Ammonia phosphate phases, stable in alkaline systems [43], formed in the internal layers only, where basic pH was preserved.
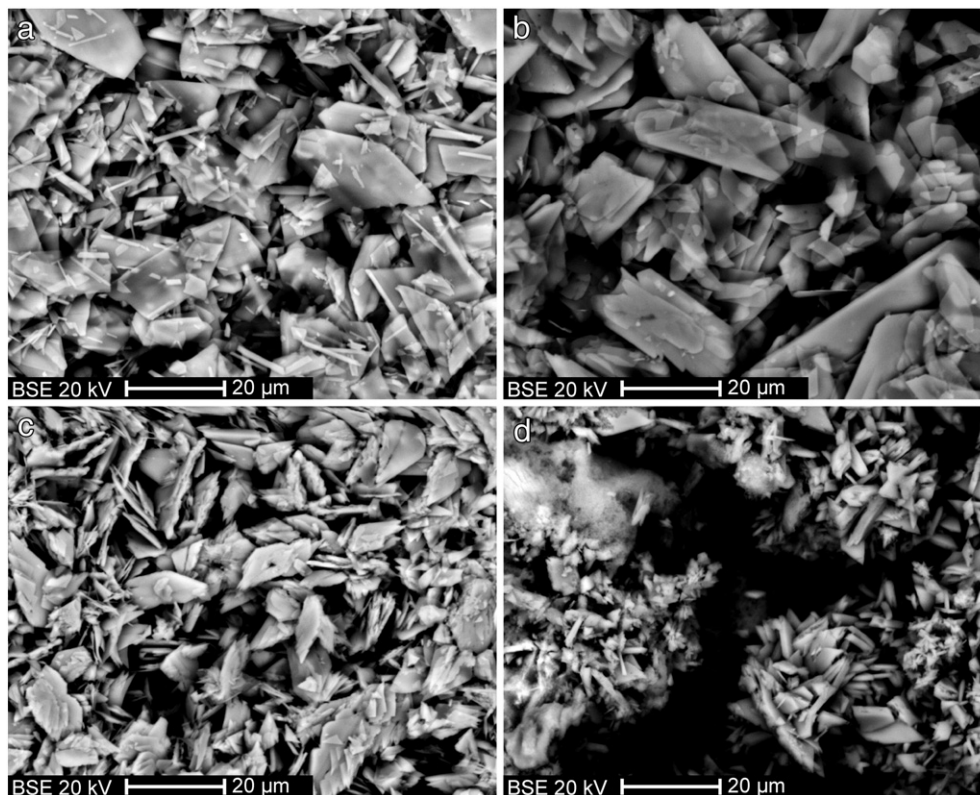
Fig. 9. SEM-BSE image of the synthesized phases: a) gypsum end-member; b) brushite end-member; c) brushite-near phase; d) ardealite-like phase.

These secondary processes were thermodynamically described with PHREEQC software (release 2.15.0), a freeware software package designed to perform low-temperature aqueous geochemical calculations [44]. Predominance and mineral stability diagrams according to pH and concentration of reactants were calculated through simulations on several simplified pore-water compositions. In Fig. 13e, supersaturation curves of phosphate and sulfate mineral phases were calculated as a function of pH at T = 25 °C and P = 1 atm, assuming that $Ca^{2+} = Mg^{2+}$ and the following solution species concentrations: $H_3PO_4 = 10$ mmol/l, $H_2SO_4 = 100$ mmol/l, $Ca^{2+} = Mg^{2+} = 30$ mmol/l, $NH_4^+ = 5$ mmol/l, NaCl = 0.1 M. The calculations confirmed that the crystallization of the secondary phases is controlled by the pH of the system. Brushite formation was favored at pH under 6, while that of octacalcium phosphate and apatite was favored at higher pH values. Furthermore, struvite showed positive supersaturation indexes at pH values over 7, while the precipitation of gypsum is not pH-dependent. Besides the model, a kinetic control on the nucleation and growth of the precursors shall be considered, in particular octacalcium phosphate [45], as the apatite crystallization rate is the lowest, which is a limiting factor in its formation within the system. Furthermore, the hypothesis of amorphous calcium phosphate occurrence in the first phases of alteration is consistent with high pH and reagent concentration, despite the meta-stability of this compound [17]. Moreover, the presence of Mg in the system from the dissolution of dolostones and magnesium limestones stabilizes the amorphous calcium phosphate and brushite, inhibiting the crystallization of apatite and less extensively of octacalcium phosphate [46].

The transformation of calcium phosphate precursors into apatite was locally inhibited by the acidic pH and the presence of stabilizing ions in solution [47]. The transformation of brushite into apatite was only partial, and occurred by epitaxial growth on seed crystals [48], leading to a higher crystallinity of the phase (Fig. 13c). In the L4 layers, a partial transformation of octacalcium phosphate into apatite occurred

both by dissolution and reprecipitation processes [49], and by epitaxial growth on seed crystals [18], leading to variable degrees of crystallinity of the phase. In the L5 layers, the conversion of amorphous calcium phosphate into apatite was more effective due to the basic pH values and, according to literature data [50], this justifies the lower apatite crystallinity.

Finally, the warming of concrete surfaces due to the exposure to maximum environmental temperatures near 40 °C during summer seasons [51] promoted a partial dehydration of the gypsum–brushite solid solution phases, and the crystallization of partially dehydrated sulfates (bassanite, β-anhydrite) and anhydrous phosphates (monetite) (Fig. 13d). At equal chemical composition (e.g. same relative proportions of the end-members), only the low crystalline fraction of the materials underwent dehydration, being more susceptible to dehydration at temperatures below 80 °C. Conversely, at equal crystallinity and varying chemical composition, the end-members and the gypsum- and brushite-rich phases of the solid solution underwent dehydration, while the phases with compositions near the respective stoichiometric compound remained hydrated, thus being more stable in that form.

5. Conclusions

This study demonstrated that the action of pollutants in aggressive environments caused a severe degradation in the concrete of the C3 building of the Ex-Agrimont area. A significant phosphate–concrete interaction was observed and verified, also thermodynamically, highlighting a form of chemical degradation not widely considered yet. Phosphate and sulfate attack resulted to be synergic, with the formation of solid solution phases. Moreover, heterogeneous sequences of crystallization and diffuse precipitation and permanence of apatite precursors were observed, strongly influenced by pH and concentration gradients and by the presence of stabilizing ions, like Mg, in pore solution. Finally,
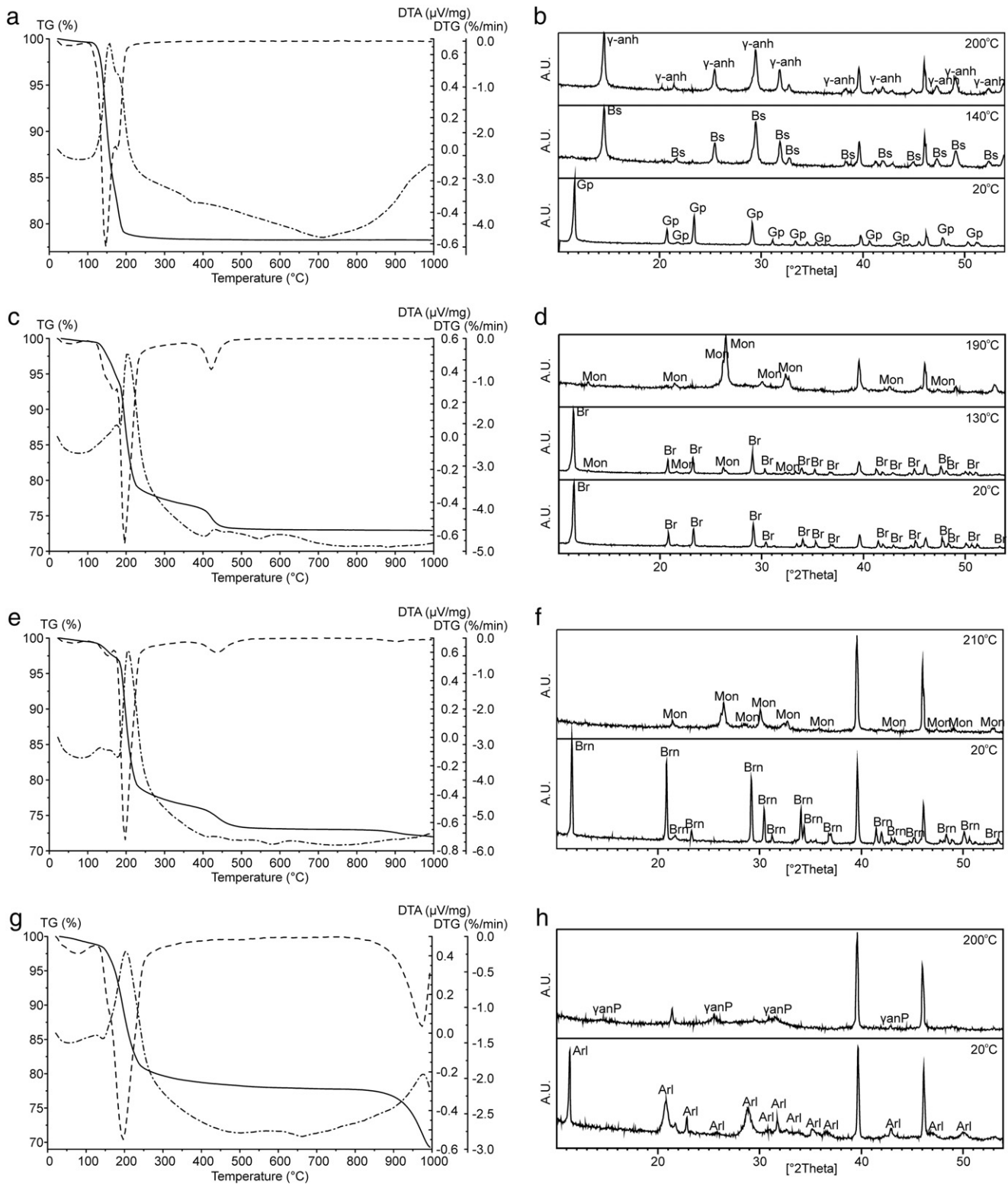
Fig. 10. Results of the in situ thermal analyses on the synthesized phases: a, c, e, g) thermogravimetric curve (solid line), derivative thermogravimetric curve (dashed line) and differential thermal curve (dotted line) for the gypsum end-member, brushite end-member, brushite-near phase and ardealite-like phase, respectively; b, d, f, h) diffraction patterns obtained during the dehydration of gypsum end-member, brushite end-member, brushite-near phase and ardealite-like phase, respectively. Peaks at 39.5° and 46° [2θ] = platinum sample holder, peak at 21° [2θ] = cristobalite impurity formed on the sample holder. Abbreviations: Arl = ardealite-like phase, Br = brushite, Brn = brushite-near phase, Bs = bassanite, γ-anh = γ-anhydrite, γanP = SO_4^{2-}-HPO_4^{2-}-substituted γ-anhydrite, Gp = gypsum, Mon = monetite.

the occurrence of anhydrous calcium phosphates and sulfates in the external layers of the altered concretes was related to dehydration phenomena of the less crystalline fractions of gypsum- and brushite-rich

phases of the gypsum–brushite solid solution, controlled by crystal size and kinetic factors. Unlike what is reported in the literature for brushite [52], dehydration of dihydrated calcium phosphate–sulfate pure end-
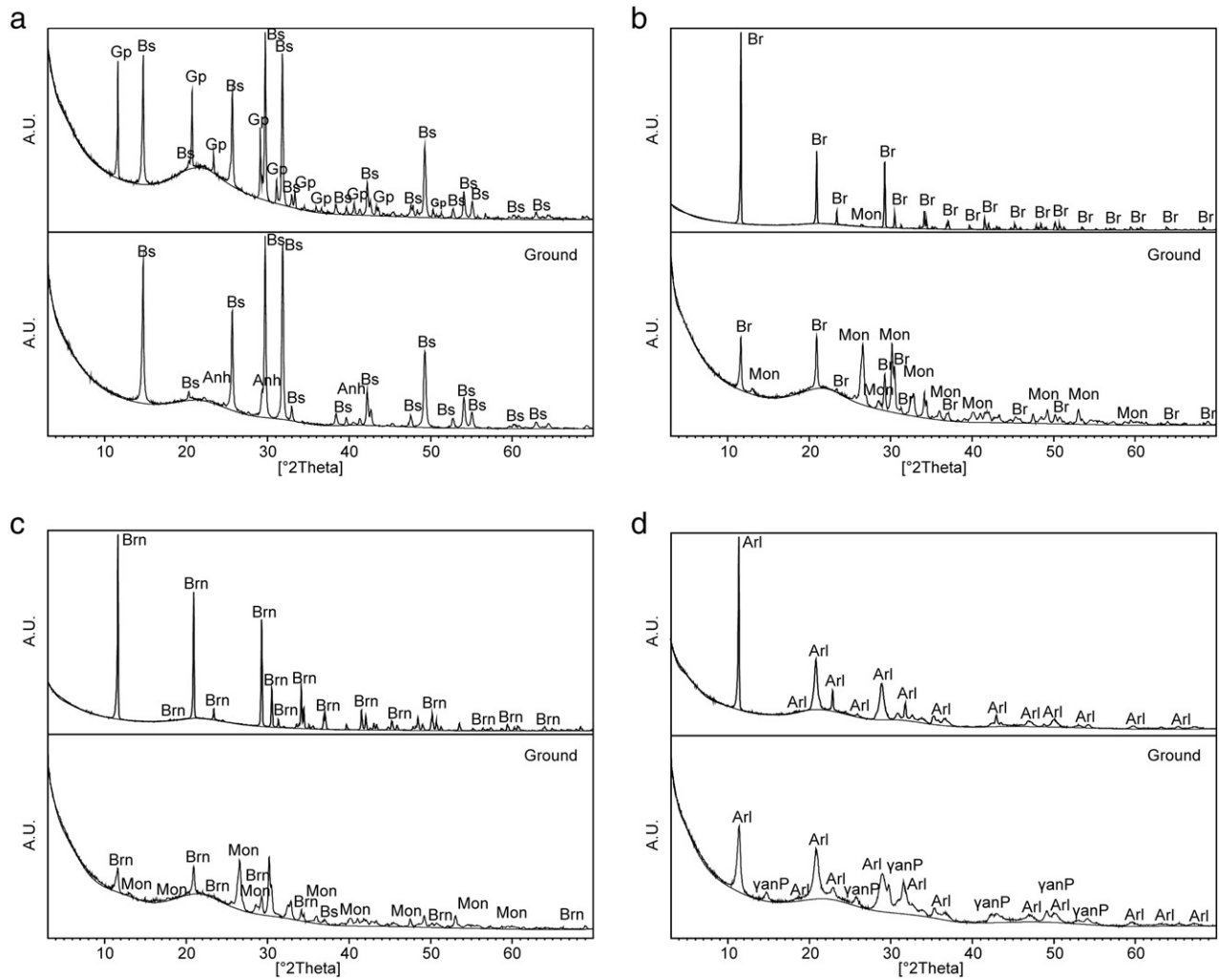
Fig. 11. Diffraction patterns of the synthesized phases after thermal treatment at 80 °C for 48 h (upper pattern) and after grinding and thermal treatment at 80 °C for 48 h (lower pattern): a) gypsum end-member; b) brushite end-member; c) brushite-near phase; d) ardealite-like phase. Abbreviations: Arl = ardealite-like phase, Br = brushite, Brn = brushite-near phase, Bs = bassanite, anh = β-anhydrite, γanP = SO_4^{2-}–HPO_4^{2-}-substituted γ-anhydrite, Gp = gypsum, Mon = monetite.

members, solid solutions, and double salt ardealite, was experimentally found to take place at relatively low temperatures (80 °C and, most likely, even lower values), mainly due to the crystallite size.

Table 4

Mineralogical composition of the synthesized phases after thermal treatment at 80 °C for 48 h and after grinding and thermal treatment at 80 °C for 48 h. As for the polycrystalline materials, the results of the semiquantitative phase analysis (expressed as wt.%) are reported, obtained by full profile fitting of the experimental XRPD patterns according to the Rietveld method (R_{wp} for each refined pattern is reported). Rietveld refinement was not performed on the ground ardealite-like sample, due to the absence of a structural model for the synthesized phase. Abbreviations: Arl = ardealite-like phase, Br = brushite, Brn = brushite-near phase, Bs = bassanite, anh = β-anhydrite, γanP = SO_4^{2-}–HPO_4^{2-}-substituted γ-anhydrite, Gp = gypsum, Mon = monetite.

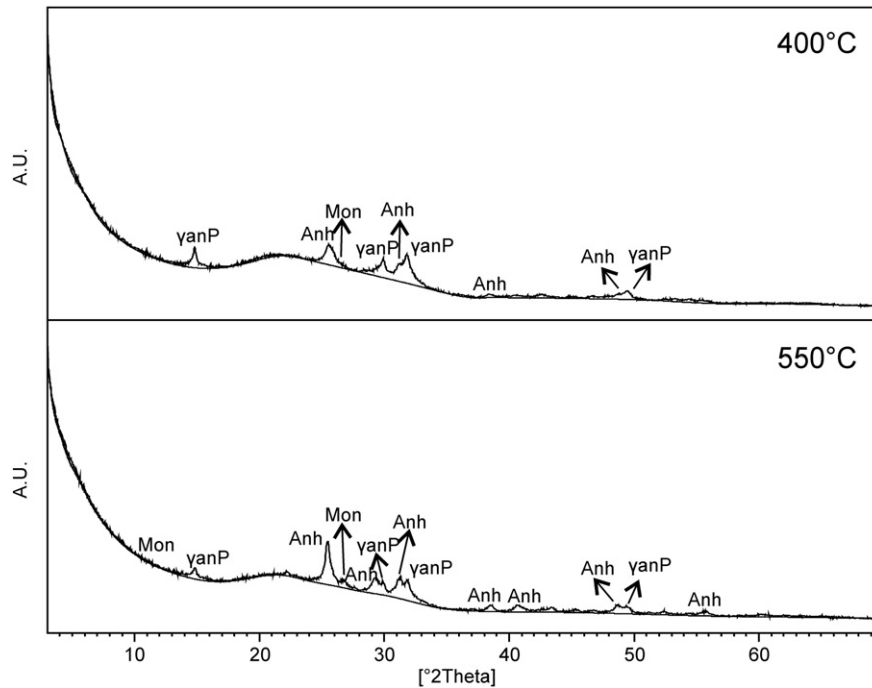| Phase	Gp	Gp, ground	Br	Br, ground	Brn	Brn, ground	Arl	Arl, ground
R_{wp}	6.01	7.75	5.61	4.10	–	4.27	–	–
Anh	–	2.7	–	–	–	–	–	–
Arl	–	–	–	–	–	–	100	Dominant
Br	–	–	96.4	37.5	–	–	–	–
Brn	–	–	–	–	100	29.9	–	–
Bs	71.9	97.3	–	–	–	0.5	–	–
γanP	–	–	–	–	–	–	–	Subordinate
Gp	28.1	–	–	–	–	–	–	–
Mon	–	–	3.6	62.5	–	69.6	–	–

Fig. 12. Diffraction patterns of the ardealite-like phase after thermal treatment for 4 h at 400 °C and 550 °C, respectively.
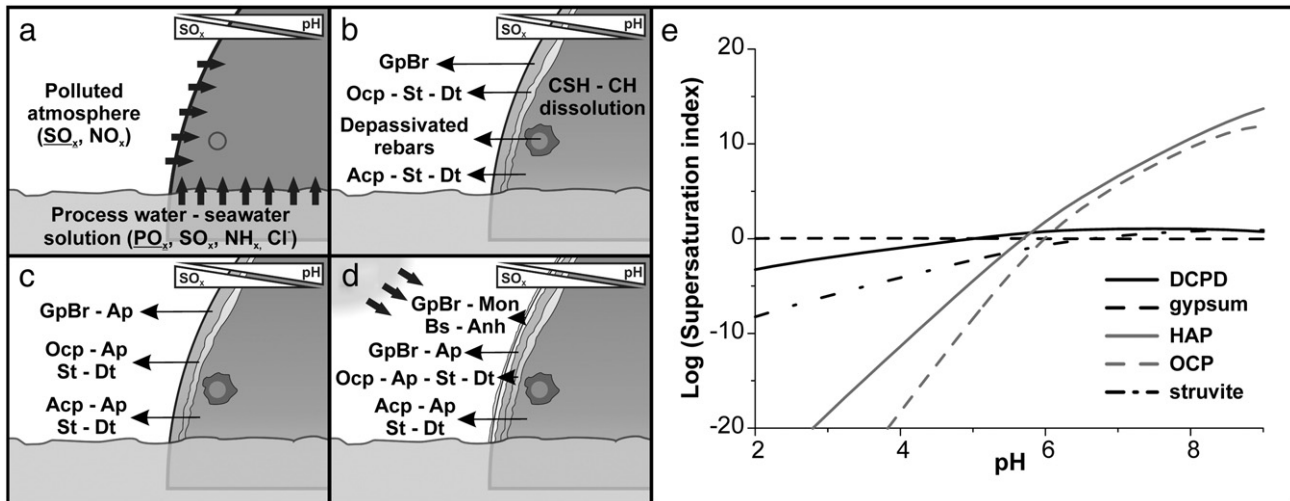

Fig. 13. Alteration model: a) action of pollutants on concrete structures; b) first alteration phase, formation of apatite precursors; c) second alteration phase, conversion of apatite precursors; d) third alteration phase, dehydration of the solid solution; e) supersaturation curves of phosphate and sulfate mineral phases as a function of pH, as determined by the thermodynamic model. Abbreviations: Acp = amorphous calcium phosphate, Anh = β-anhydrite, Ap = apatite, Bs = bassanite, Dt = dittmarite, GpBr = gypsum–brushite solid solution, Mon = monetite, Ocp = octacalcium phosphate, St = struvite.

References

[1] F.P. Glasser, J. Marchand, E. Samson, Durability of concrete − Degradation phenomena involving detrimental chemical reactions, Cem. Concr. Res. 38 (2008) 226–246.
[2] J.M. Tulliani, L. Montanaro, A. Negro, M. Collepardi, Sulfate attack of concrete building foundations induced by sewage waters, Cem. Concr. Res. 32 (2002) 843–849.
[3] N. Marinoni, M. Pellizon Birelli, C. Rostagno, A. Pavese, The effects of atmospheric multipollutants on modern concrete, Atmos. Environ. 37 (2003) 4701–4712.
[4] J.P. Skalny, I. Odler, J. Marchand, Sulfate Attack on Concrete, Spon Press, New York, 2001.
[5] M. Collepardi, A state-of-the art review on delayed ettringite attack on concrete, Cem. Concr. Compos. 25 (2003) 401–407.

[6] A. Neville, The confused world of sulfate attack on concrete, Cem. Concr. Res. 34 (2004) 1275–1296.

[7] V. Zivica, A. Bajza, Acidic attack of cement based materials a review. Part 1. Principle of acidic attack, Constr. Build. Mater. 15 (2001) 331–340.

[8] V. Zivica, A. Bajza, Acidic attack of cement-based materials—A review Part 2. Factors of rate of acidic attack and protective measures, Constr. Build. Mater. 16 (2002) 215–222.

[9] V. Zivica, Acidic attack of cement based materials — A review Part 3: research and test methods, Constr. Build. Mater. 18 (2004) 683–688.

[10] E. Roziere, A. Loukili, R. El Hachem, F. Grondin, Durability of concrete exposed to leaching and external sulphate attacks, Cem. Concr. Res. 39 (2009) 1188–1198.

[11] Z. Amjad, Calcium Phosphates in Biological and Industrial Systems, Springer US, New York, 1997.

[12] M.J. Kohn, J. Rakovan, J.M. Hughes, Phosphates: Geochemical, Geobiological, and Materials Importance, Mineralogical Society of America and Geochemical Society, Washington D.C., 2002.

[13] R.B. Heimann, Calcium Phosphate: Structure, Synthesis, Properties, and Applications, Nova Publishers, Hauppauge, 2014.

[14] A.M. Neville, J.J. Brooks, Concrete Technology, John Wiley and Sons, New York, 1990.

[15] D.J. Naus, L.R. Dole, C.H. Mattus, Laboratory investigation on effect of phosphate ions on concrete, Report to the US NRC, Oak Ridge National Laboratory, Oak Ridge, 2006.

[16] J.D. Miller, A.D. Randolph, G.W. Drach, Observations upon calcium oxalate crystallization kinetics of simulated urine, J. Urol. 117 (1977) 342–345.

[17] M.S.A. Johnsson, G.H. Nancollas, The role of brushite and octacalcium phosphate in apatite formation, Crit. Rev. Oral Biol. Med. 3 (1/2) (1992) 61–82.

[18] L.C. Chow, E.D. Eanes, Octacalcium Phosphate, Karger Publishers, Basel, 2001.

[19] T. Sakae, H. Nagata, T. Sudo, The crystal structure of synthetic calcium phosphate–sulfate hydrate, $Ca_2(HPO_4)(SO_4) \cdot 4H_2O$, and its relation to brushite and gypsum, Am. Mineral. 63 (1978) 520–527.

[20] C. Rinaudo, A.M. Lanfranco, M. Franchini-Angela, The system $CaHPO_4 \cdot 2H_2O$–$CaSO_4 \cdot 2H_2O$: crystallization from calcium phosphate solutions in the presence of SO_4^{2-}, J. Cryst. Growth 142 (1994) 184–192.

[21] A.J. Pinto, A. Jimenez, M. Prieto, Thermodynamics of the gypsum–brushite–H_2O system, Rev. Soc. Esp. Mineral. 9 (2008) 193–194.

[22] A.J. Pinto, J. Carneiro, D. Katsikopoulos, A. Jimenez, M. Prieto, The link between brushite and gypsum: miscibility, dehydration, and crystallochemical behavior in the $CaHPO4 \cdot 2H_2O$–$CaSO4 \cdot 2H_2O$ system, Cryst. Growth Des. 12 (2012) 445–455.

[23] C.L. Roberts-Wollman, J.E. Breen, J. Cawrse, Measurements of thermal gradients and their effects on segmental concrete bridge, J. Bridg. Eng. 7 (2002) 166–174.

[24] F.M. Lea, The action of ammonium salts on concrete, Mag. Concr. Res. 17 (52) (1965) 115–116.

[25] R. Jauberthie, F. Rendell, Physicochemical study of the alteration surface of concrete exposed to ammonium salts, Cem. Concr. Res. 33 (2003) 85–91.

[26] U. Schneider, S.W. Chen, Deterioration of high-performance concrete subjected to attack by the combination of ammonium nitrate solution and flexure stress, Cem. Concr. Res. 35 (2005) 1705–1713.

[27] A. Whitaker, J.W. Jeffery, The crystal structure of struvite, $MgNH_4PO_4 \cdot 6H_2O$, Acta Crystallogr. B 26 (1970) 1429–1440.

[28] J.D. Doyle, S.A. Parsons, Struvite formation, control and recovery, Water Res. 36 (2002) 3925–3940.

[29] J.O. Nriagu, C.I. Dell, Diagenetic formation of iron phosphates in recent lake sediments, Am. Mineral. 59 (1974) 934–946.

[30] C. Chinello, Storia di uno sviluppo capitalistico: Porto Marghera e Venezia 1951–1973, Editori Riuniti, Roma, 1975.

[31] L. Tomiato, A. Zanardini, Rapporto ambientale d'area di Porto Marghera: bilancio ambientale 1998–2004, ARPA, Venezia, 2005.

[32] M. Daigle, Phosphate Primer [on-line], Florida Institute of Phosphate ResearchOn: [Accessed 1st September 2014] http://www1.fipr.state.fl.us/PhosphatePrimer.

[33] M. Secco, Characterization Studies on Cement Conglomerates from Historic Reinforced Concrete Structures, Department of Geosciences, University of Padova, 2012. (PhD Thesis).

[34] M.C. Schlegel, U. Mueller, U. Panne, F. Emmerling, Deciphering the sulfate attack of cementitious materials by high-resolution micro-X-ray diffraction, Anal. Chem. 83 (2011) 3744–3749.

[35] O. Paris, C. Li, S. Siegel, G. Weseloh, F. Emmerling, H. Riesemeier, A. Erko, P. Fratzl, A new experimental station for simultaneous X-ray microbeam scanning for small- and wide-angle scattering and fluorescence at BESSY II, J. Appl. Crystallogr. 40 (2007) 466–470.

[36] P. Stutzman, Scanning electron microscopy imaging of hydraulic cement microstructure, Cem. Concr. Compos. 26 (2004) 957–966.

[37] H.M. Rietveld, A profile refinement method for nuclear and magnetic structures, J. Appl. Crystallogr. 2 (1969) 65–71.

[38] C.A. Strydom, D.L. Hudson-Lamb, J.H. Potgieter, E. Dagg, The thermal dehydration of synthetic gypsum, Thermochim. Acta 269 (270) (1995) 631–638.

[39] A.O. McIntosh, W.L. Jablonski, X-ray diffraction powder patterns of the calcium phosphates, Anal. Chem. 28 (9) (1956) 1424–1427.

[40] M. Benzoni, L. Berti, D. Bon, A. Girolimetto, M. Novello, Monitoraggio delle Acque di Transizione della Regione Veneto, ARPA, Venezia, 2013.

[41] A. Pourbaix, Localized corrosion: behaviour and protection mechanisms, in: A. Turnbull (Ed.), Corrosion Chemistry within Pits, Crevices and Cracks, National Physical Laboratory, Teddington, Middlesex, 1984, pp. 1–15.

[42] U. Angst, Chloride Induced Reinforcement Corrosion in Concrete, Department of Structural Engineering, Norwegian University of Science and Technology, 2011. (PhD Thesis).

[43] A.W. Taylor, A.W. Frazier, E.L. Gurney, J.P. Smith, Solubility products of di-and trimagnesium ammonium and dissociation of magnesium phosphate solutions, Trans. Faraday Soc. 59 (1963) 1585–1589.

[44] D.L. Parkhurst, C.A.J. Appelo, *User's guide to PHREEQC (version 2)* — A computer program for speciation, reaction-path, 1D-transport, and inverse geochemical calculations, US Geological Survey Water-Resources Investigations Report, 99-4259, 1999, pp. 1–312.

[45] J.C. Heughebaert, G.H. Nancollas, Kinetics of crystallization of octacalcium phosphate, J. Phys. Chem. 88 (1984) 2478–2481.

[46] M.H. Salimi, J.C. Heughebaert, G.H. Nancollas, Crystal growth of calcium phosphate in the presence of magnesium ions, Langmuir 1 (1985) 119–122.

[47] J.J. Vogel, Calcium phosphate solid phase induction by dioleoylphosphatidate liposomes, J. Colloid Interface Sci. 111 (1986) 152–159.

[48] P.G. Koutsoukos, G.H. Nancollas, Crystal growth of calcium phosphates. Epitaxial considerations, J. Cryst. Growth 53 (1981) 10–19.

[49] B.B. Tomazic, M.S. Tung, T.M. Gregory, W.E. Brown, Mechanism of hydrolysis of octacalcium phosphate, Scan. Electron Microsc. 3 (1989) 119–127.

[50] J.E. Harries, D.W.L. Hukins, C. Holt, S.S. Hasnain, Conversion of amorphous calcium phosphate into hydroxyapatite, J. Cryst. Growth 84 (1987) 563–570.

[51] M. Zane, E. Zanotto, G. Chiellino, ATTIVITÀ IPPC 6.4 b) - Trattamento e trasformazione destinati alla fabbricazione di prodotti alimentari a partire da materie prime vegetali con una capacità di produzione di prodotti finiti di oltre 300 tonnellate al giorno, Allegato D5: Relazione tecnica su dati meteoclimatici, eAmbiente, Venezia, 2013.

[52] P.F. Schofield, K.S. Knight, J.A.M. Van der Houwen, E. Valsami-Jones, The role of hydrogen bonding in the thermal expansion and dehydration of brushite, di-calcium phosphate dihydrate, Phys. Chem. Miner. 31 (9) (2004) 606–624.